A novel CuAl$_2$O$_4$/MoS$_2$/BaFe$_{12}$O$_{19}$ magnetic photocatalyst simultaneously coupling type I and Z-scheme heterojunctions for the sunlight-driven removal of tetracycline hydrochloride

Mengjun Han[a)], Shifa Wang[a)]*, Xinmiao Yu[a)], Xianlun Yu[a)], Huajing Gao[b)], Xianju Zhou[b)], Dengfeng Li[b)], Leiming Fang [c)], Jagadeesha Angadi.V[d)], Mohd Ubaidullah[e)], Bidhan Pandit[f)]

[a)]School of Electronic and Information Engineering, Chongqing Three Gorges University, Chongqing, Wanzhou, 404000, China.

*e-mail: wangshifa2006@yeah.net (Shifa Wang)

[b)]School of Science, Chongqing University of Posts and Telecommunications, Nan'an District, 400065 Chongqing, China.

[c)] Institute of Nuclear Physics and Chemistry, China Academy of Engineering Physics, Sichuan, Mianyang, 621900, China.

[d)] Department of Physics, P.C. Jabin Science College, Hubballi – 580031 Karnataka, India.

[e)] Department of Chemistry, College of Science, King Saud University, P.O. Box 2455, Riyadh 11451, Saudi Arabia.

[f)] Department of Materials Science and Engineering and Chemical Engineering, Universidad Carlos III de Madrid, Avenida de la Universidad 30, 28911 Leganés, Madrid, Spain.

S1 Experimental Section

S1.1 Materials

The laminar MoS_2 is purchased from Aladdin Chemical Reagent Network. Copper nitrate trihydrate ($Cu(NO_3)_2 \cdot 3H_2O$, 99%), aluminum nitrate nonahydrate ($Al(NO_3)_3 \cdot 9H_2O$, 99.9%), barium nitrate ($Ba(NO_3)_2$), iron nitrate nonahydrate ($Fe(NO_3)_3 \cdot 9H_2O$ (99.9%)), citric acid ($C_6H_8O_7$, 99.5%), glucose ($C_6H_{12}O_6 H_2O$, 99%), acrylamide (C_3H_5NO, AR), and N, N'-methylene-bisacrylamide ($C_7H_{10}N_2O_2$, 99%) were purchased from Eco Reagent Co., LTD, Chengdu and used without further purification.

S1.2 Synthesis of spinel $CuAl_2O_4$ oxides

According to the formula $CuAl_2O_4$, stoichiometric amounts of $Cu(NO_3)_2 \cdot 3H_2O$ and $Al(NO_3)_3 \cdot 9H_2O$ were dissolved in the distilled water to obtain a solution of 0.015 mol/L. The mole ratio of Cu to Al is 1:2. After the above solution was transparent, 4.7282 g citric acid is weighed to chelate Cu and Al ions. Subsequently, the 20 g glucose, 9.5958 g acrylamide and 1.9192 g N, N'-methylene-bisacrylamide were dissolved in the solution. The citric acid, glucose and N, N'-methylene-bisacrylamide are used as chelating agent, agent to prevent gel collapse and cross-linking agent, respectively. The molar ratio of citric acid to metal ions, the content of glucose, the molar ratio of acrylamide to metal ions, the molar ratio of acrylamide to N, N'-methylene-bisacrylamide are 1.5:1, 20 g, 9:1 and 5:1, respectively. All the above experimental steps were carried out under the action of magnetic stirring. After the above reagents were completely dissolved, the solution was heated to 90 °C, and jelly-like gel was obtained after a period of time. The jelly-like gel was dried at 120 °C for 24 h in a thermostat drier to obtain a xerogel. The xerogel was ground into powder and some powder was sintered for 5 h in air at 800 °C to obtain spinel $CuAl_2O_4$ oxides.

S1.3 Synthesis of spinel BaFe$_{12}$O$_{19}$ (BFO) magnetic photocatalysts

A similar method was used to prepare BaFe$_{12}$O$_{19}$ (BFO) magnetic photocatalysts. There are three differences from the synthesis of BST5 photocatalysts: (1) In the synthesis process, (Ba(NO$_3$)$_2$) and iron nitrate nonahydrate (Fe(NO$_3$)$_3$·9H$_2$O (99.9%)) were used as barium and iron salts, respectively. (2) BFO xerogel was sintered at 900 °C for 5 hours to obtain the BFO magnetic photocatalysts. (3) The mole ratio of Ba to Fe is 1:12.

S1.4 Synthesis of CuAl$_2$O$_4$/MoS$_2$ composite photocatalysts

According to mass ratio of CuAl$_2$O$_4$ and MoS$_2$, weighing CuAl$_2$O$_4$ and MoS$_2$ and grinding them in mortar for 1 h, and then calcining them in tubular furnace at 200 °C for 2 h, CuAl$_2$O$_4$/MoS$_2$ composite photocatalysts with the mass percentage of MoS$_2$ of 5 wt%, 10 wt%, 15 wt% and 20 wt% were obtained. They are labeled CAO/5%MS, CAO/10%MS, CAO/15%MS and CAO/20%MS, respectively.

S1.5 Material characterization

The crystallographic properties of CAO/MS/BFO magnetic photocatalysts were measured by the means of DX-2007BH X-ray powder diffraction (XRD) with Cu Kα radiation at a wavelength of 1.5406 Å operated at 40 kV and 30 mA. The functional group information of CAO/MS/BFO magnetic photocatalysts were characterized by a FTIR 650 type Fourier transform infrared (FTIR) spectrophotometer with the wave-number range of 400−4000 cm^{-1}. The hysteresis loop of CAO/MS/BFO magnetic photocatalysts were measured by a Quantum Design Physical Properties Measurement System (PPMS) at room temperature. The XPS signals of CAO/MS/BFO magnetic photocatalysts were measured by a KRATOS X SAM 800 X-ray photoelectron spectrometer (XPS). The surface micro-structures of CAO/MS/BFO magnetic photocatalysts were observed by a Thermo Scientific™

field-emission scanning electron microscopy (FE-SEM) and JEM 2100F transmission electron microscopy (TEM). Ultraviolet-visible diffuse reflectance spectra (UV-vis DRS) of CAO/MS/BFO magnetic photocatalysts were measured by a UV1901 UV-visible spectrophotometer with the $BaSO_4$ used as reference. UV-Vis absorption spectra (ABS) of CAO/MS/BFO magnetic photocatalysts were obtained on ths basis of the UV-vis DRS and the Kubelka-Munk (K–M) formula,

$$F(R) = \frac{\alpha}{S} = \frac{(1-R_{\infty})^2}{2R} \qquad (S1)$$

Where, R, α and S are the reflectance, the absorption coefficient and the scattering coefficient of CAO/MS/BFO magnetic photocatalysts, respectively.

S1.6 Photocatalytic experiments

To study the photocatalytic activity of CAO/MS/BFO magnetic photocatalysts and explore the influence of different mass percentage of BFO on the photocatalytic activity of CAO/MS/BFO magnetic photocatalysts, tetracycline hydrochloride (TC) was selected as the target degradation antibiotic to complete the related photocatalytic experiments. The initial antibiotic concentration, catalyst content and pH value were 50-200 mg/L, 0.25-1.5 g/L and 3-13, respectively. In the photocatalytic experiment, xenon lamp is used to simulate sunlight. Before the photocatalytic experiment, the adsorption experiments were performed and stirred in dark conditions for 30 min to achieve adsorption equilibrium. Then the solution was reacted with the simulate sunlight and stirred for 180 min, and a sample was taken every 30 min. After the experiment, the obtained sample was centrifuged for 15 min. Finally, the upper clarified liquid was taken and the absorbance curve was measured by a UV-1800 UV-visible spectrophotometer.

Capture experiments were performed to confirm the contribution of holes (h_{VB}^+), hydroxyl radicals (•OH) and superoxide radicals (•O_2^-) to photocatalysis and detected

by the disodium ethylenediamine tetraacetic acid (EDTA-2Na), 2-propanol (IPA) and 1, 4-benzoquinone (BQ) as scavengers, respectively. The process was similar to the photocatalytic experiment, except that 1 mmol/L of scavenger was added to the reaction solution. The oxygen vacancy, •OH and •O_2^- are also confirmed by the electron spin resonance (ESR)/electron paramagnetic resonance (EPR) experiments on the basis of a Bruker A300 spectrometer. The oxygen vacancy was detected at room temperature with the X-band (9.34 GHz). Spin-trapping reagents of 5-tert-butoxycarbonyl 5-methyl-1-pyrroline N-oxide (BMPO) was used to detect •O_2^-, while 5,5-dimethyl-1-pyrroline N-oxide (DMPO) was used to detect •OH. High-performance liquid chromatography-tandem mass spectrometry (HPLC–MS) were performed for the explore degradation ways and products by a positive ionization mode with a full scan range from m/z 50 to 1000. The injection volume was 10 uL and the mobile phase was A (0.1% formic acid aqueous solution) and B (0.1% formic acid methanol solution) at a flow rate of 0.8 mL•min^{-1}.
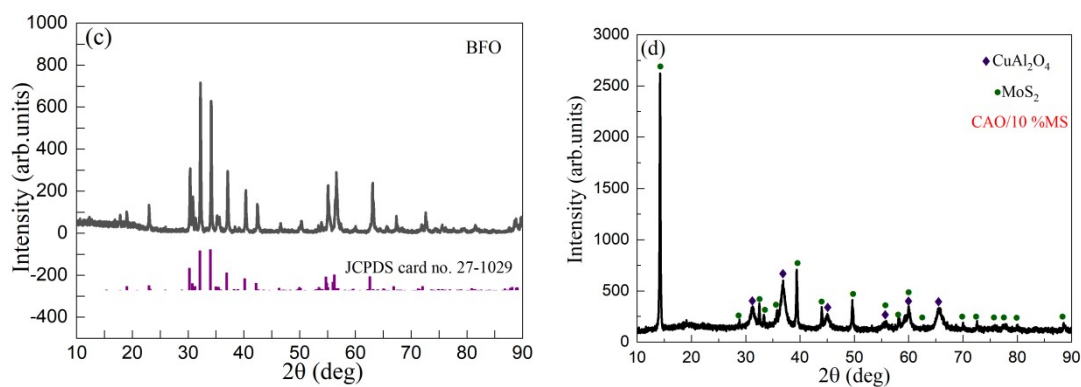
S2 XRD analysis
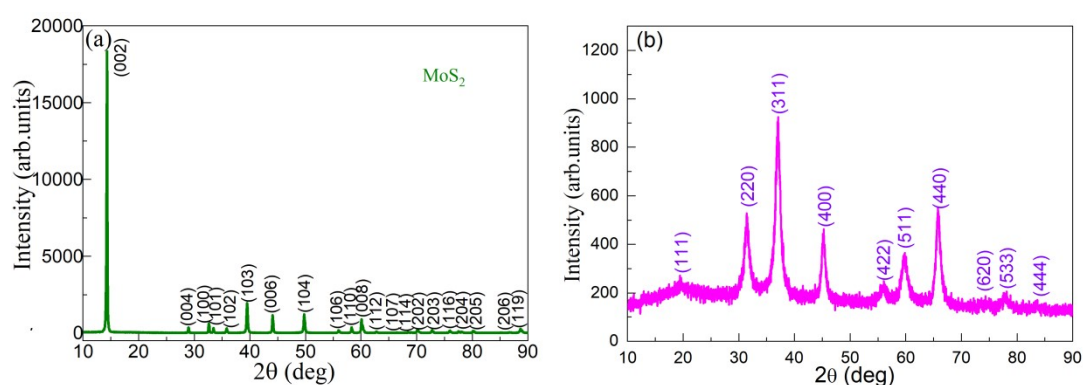
Figure S1 XRD patterns of (a) MS, (b) CAlO, (c) BFO and (d) CAO/10%MS$_2$.
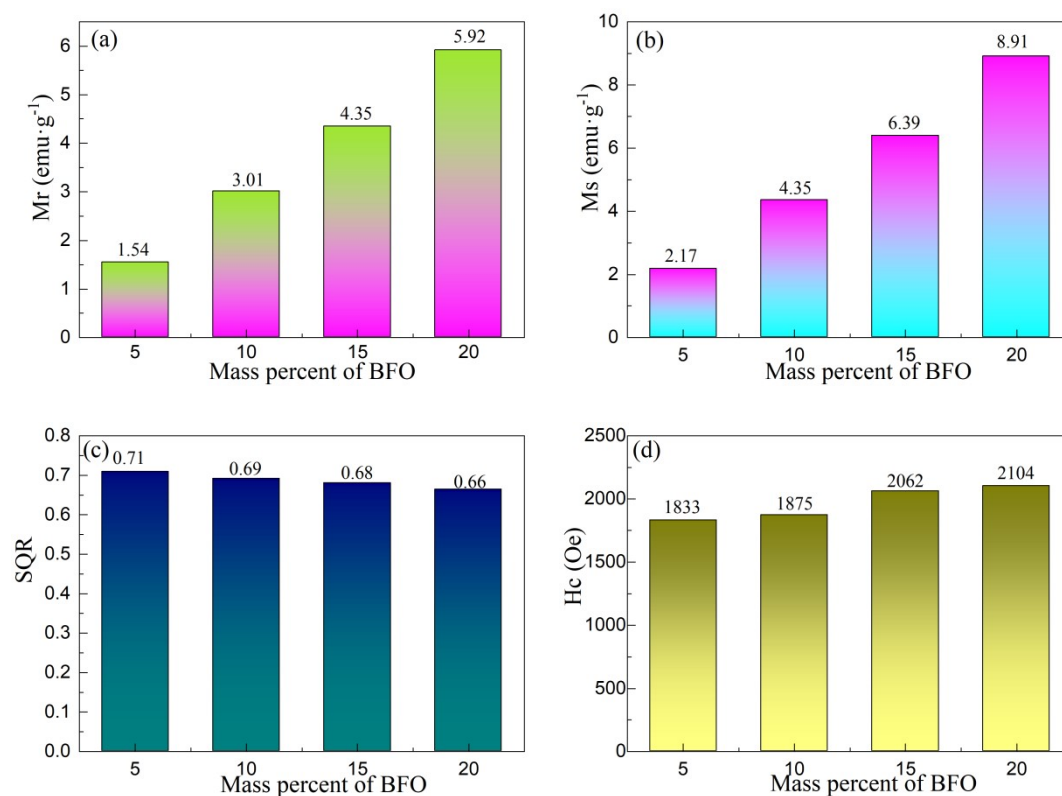
S3 Magnetic properties

Figure S2 (a) Remanent magnetization (Mr), (b) saturation magnetization (Ms), (c) squareness ratio (SQR), and (d) coercivity (Hc) of the CAO/MS/BFO magnetic photocatalysts.
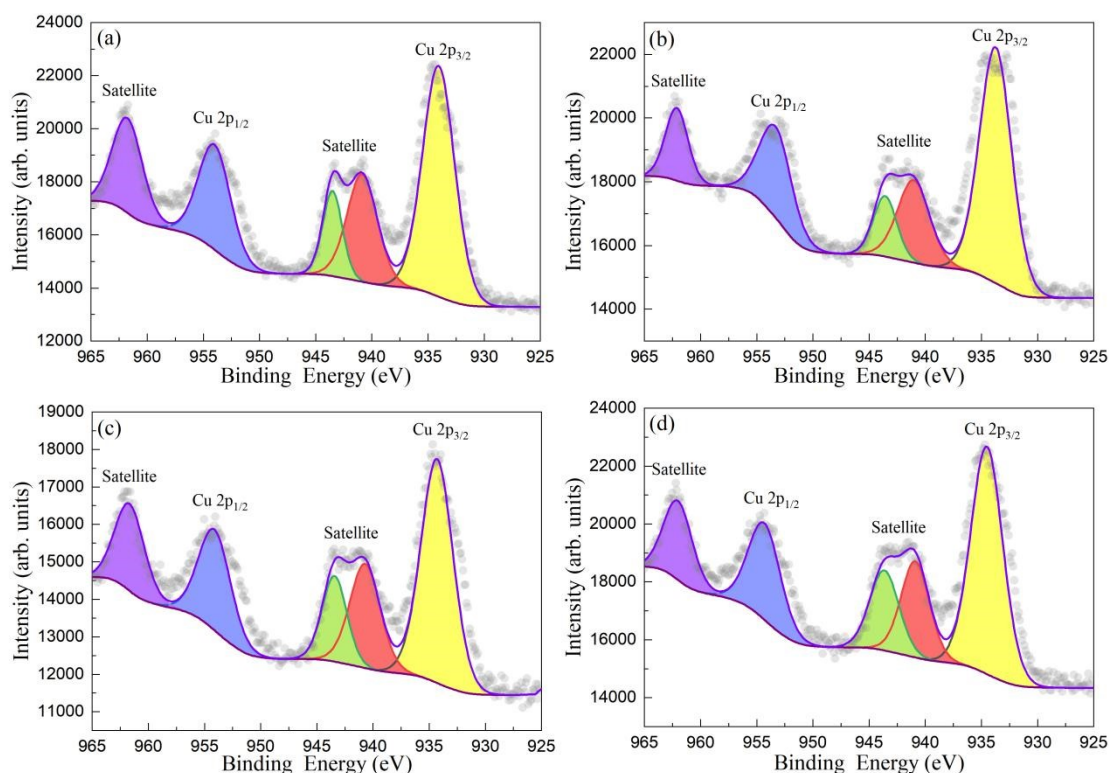
S4 XPS analysis

Figure S3 High-resolution Cu 2p XPS spectra of CAO/MS/BFO magnetic

photocatalysts. (a) CAO/MS/5%BFO, (b) CAO/MS/10%BFO, (c) CAO/MS/15%BFO

and (d) CAO/MS/20%BFO.

Figure S3 shows the high-resolution Cu 2p XPS spectra of CAO/MS/BFO magnetic

photocatalysts. The corresponding binding energy data are given in Table S1. Two

characteristic peaks are observed at 933.74-964.51 and 955.33-954.32 eV of Cu 2p3/2

and Cu 2p1/2, respectively and other three peaks are at 940.72-941.03, 943.43-943.64

and 961.66-962.12 eV could be ascribed to the satellite peak. [S1] The result further

confirmed the valence state of Cu^{2+} in $CuAl_2O_4$ is +2 due to the splitting of the Cu 2p

doublet is about 20 eV. [S2]

Table S1 The binding energies of Cu 2p, Al 2p and O 1s of CAO/MS/BFO magnetic

photocatalysts.

Sample	Cu 2p (eV)	Al 2p (eV)	O 1s (eV)

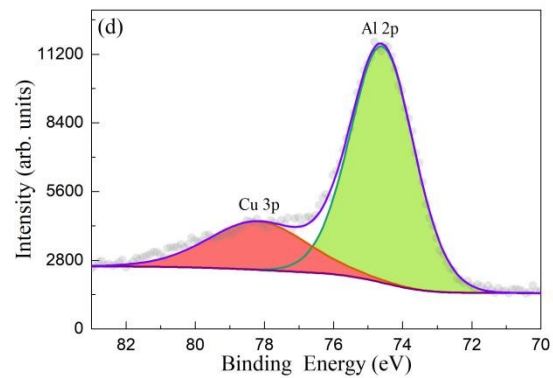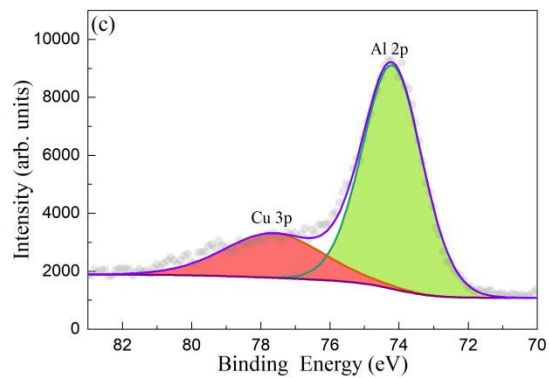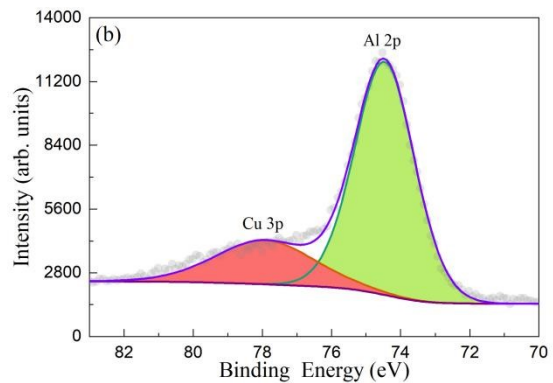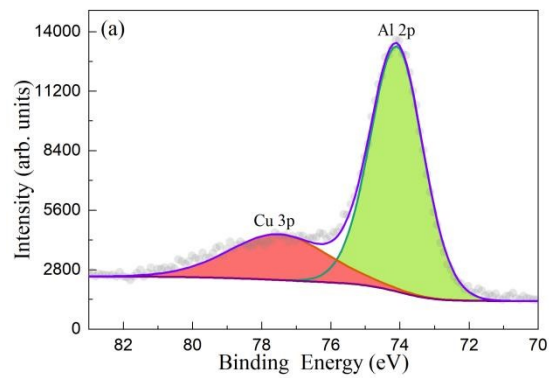|	Cu 2p$_{1/2}$	Cu 2p$_{3/2}$	Satellite	Al 2p	Cu 3p	O$_A$	O$_{Def}$	O$_{LCAO}$	O$_{BFO}$
CAO/MS/ 5%BFO	954.00	934.06	961.75 943.50 940.86	74.10	77.52	533.99	531.89	530.70	528.98
CAO/MS/ 10%BFO	953.33	933.74	962.12 943.57 941.03	74.47	77.93	533.96	532.22	530.94	528.87
CAO/MS/ 15%BFO	954.11	934.30	961.66 943.43 940.72	74.20	77.64	533.83	532.00	530.75	528.92
CAO/MS/ 20%BFO	954.32	934.51	962.00 943.64 940.89	74.60	78.19	533.86	532.31	531.05	529.07

Figure S4 High-resolution Cu 3p and Al 2p spectra of CAO/MS/BFO magnetic

photocatalysts. (a) CAO/MS/5%BFO, (b) CAO/MS/10%BFO, (c) CAO/MS/15%BFO

and (d) CAO/MS/20%BFO.

Figure S4 shows the high resolution Al 2p spectrum of CAO/MS/BFO magnetic

photocatalysts. The characteristic peaks of Al 2p spectrum can be fitted to Al 2p and

Cu 3p components by Avantage software. The Al 2p orbital located at 74.10-74.60 eV
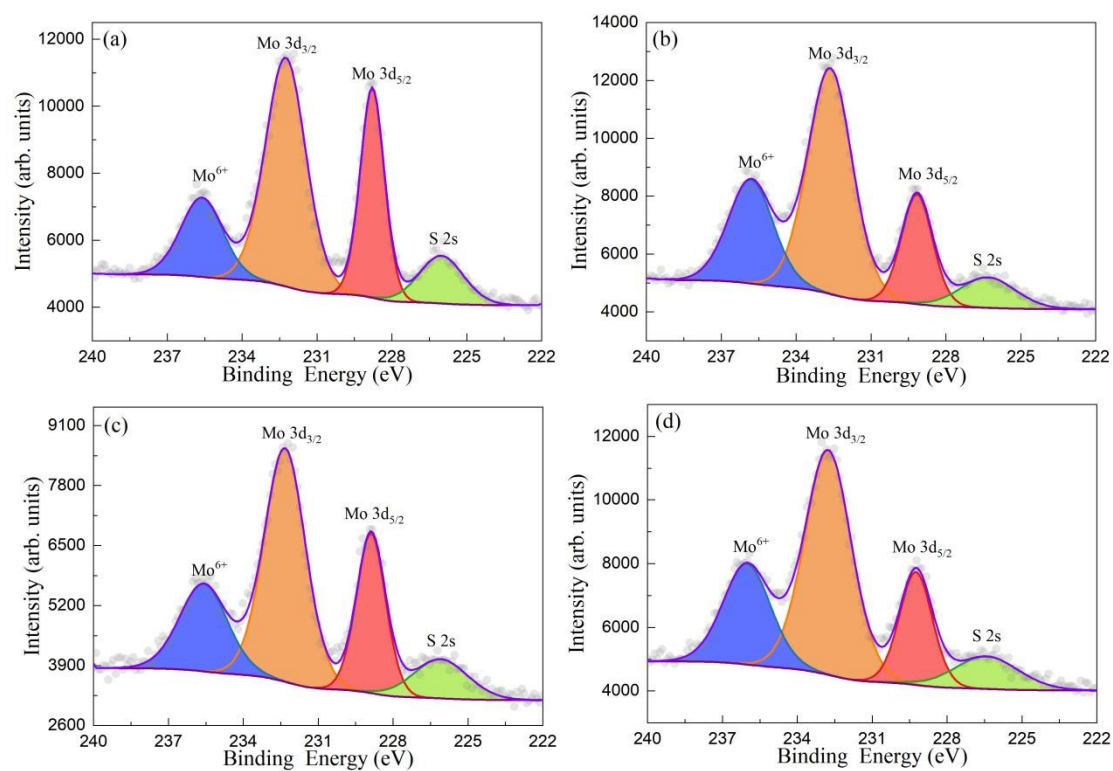
can be assigned to the Al–O–Cu of $CuAl_2O_4$.

Figure S5 High-resolution Mo 3d and S 2s spectra of CAO/MS/BFO magnetic

photocatalysts. (a) CAO/MS/5%BFO, (b) CAO/MS/10%BFO, (c) CAO/MS/15%BFO

and (d) CAO/MS/20%BFO.

The high resolution Mo 3d and S 2s spectra, as shown in Figure S5, four

predominant peaks at 235.59-236.02, 232.25-232.76, 228.79-229.25 and 226.02-

226.42 eV are ascribed to the defects on the crystal plane of the MS nanospheres, the

doublet Mo 3d3/2 and Mo 3d5/2 of Mo^{4+} ions in MS and S 2s in MS, respectively. [S3] Figure S6 displays the high-resolution S 2p spectra of CAO/MS/BFO magnetic photocatalysts, where three characteristic peaks at 168.74-169.36, 162.63-163.03 and 161.55-161.99 eV can be assigned to the S_2^{2-}, S 2p1/2 and S 2p3/2 of S^{2-} ions in MS, respectively, because of the spin orbit separation of sulfur element. [S4] The presence of S^{2-} and S_2^{2-} ions confirms that MS has been successfully hybridized with $CuAl_2O_4$ materials.

Table S2 The binding energies of Mo 3d, S 2p, Ba 3d and Fe 2p of CAO/MS/BFO magnetic photocatalysts.

| Sample	Mo 3d (eV)				S 2p (eV)			Ba 3d (eV)		Fe 2p (eV)	
	Mo^{6+}	Mo $3d_{3/2}$	Mo $3d_{5/2}$	S 2s	S_2^{2-}	S $2p_{1/2}$	S $2p_{3/2}$	Ba $3d_{3/2}$	Ba $3d_{5/2}$	Fe $2p_{1/2}$	Fe $2p_{3/2}$
CAO/MS/ 5%BFO	235.61	232.25	228.79	226.02	168.74	162.63	161.55	795.15	779.96	724.47	711.14
CAO/MS/ 10%BFO	235.82	232.63	229.16	226.32	169.07	163.03	161.90	795.17	779.81	725.56	711.84
CAO/MS/ 15%BFO	235.59	232.33	228.88	226.10	168.90	162.85	161.66	794.78	780.11	724.90	711.90
CAO/MS/ 20%BFO	236.02	232.76	229.25	226.42	169.36	163.01	161.99	794.96	780.02	725.06	711.78
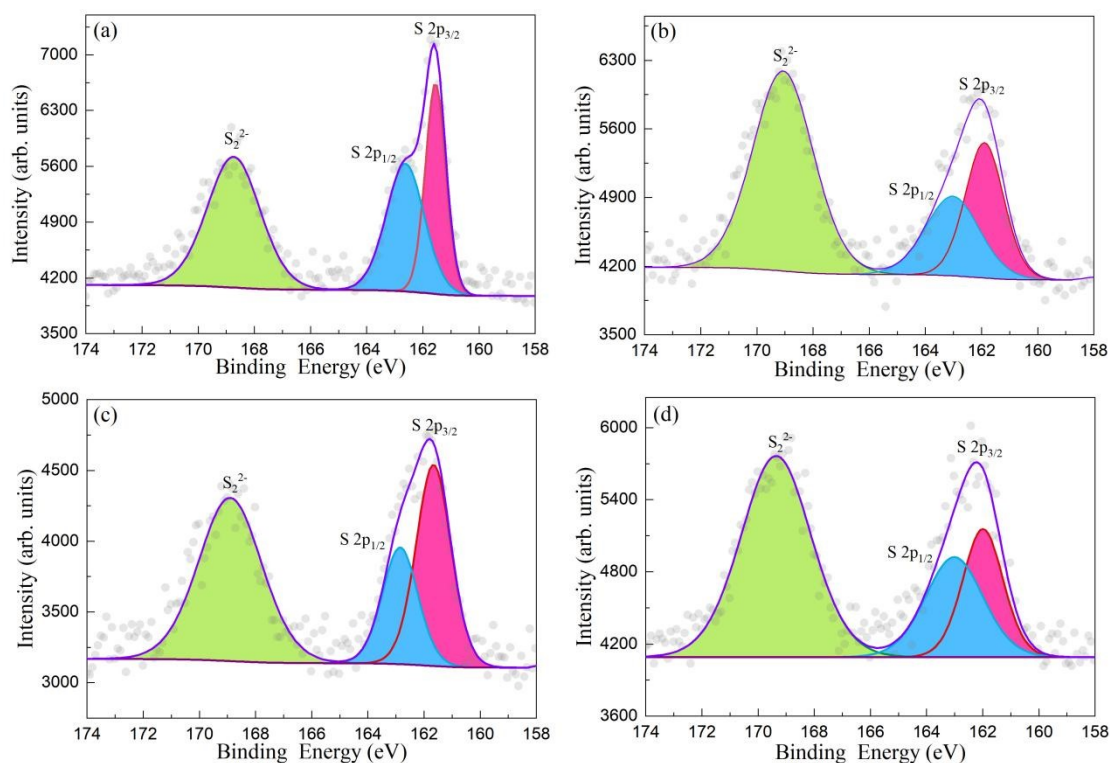
Figure S6 High-resolution S 2p spectra of CAO/MS/BFO magnetic photocatalysts. (a)

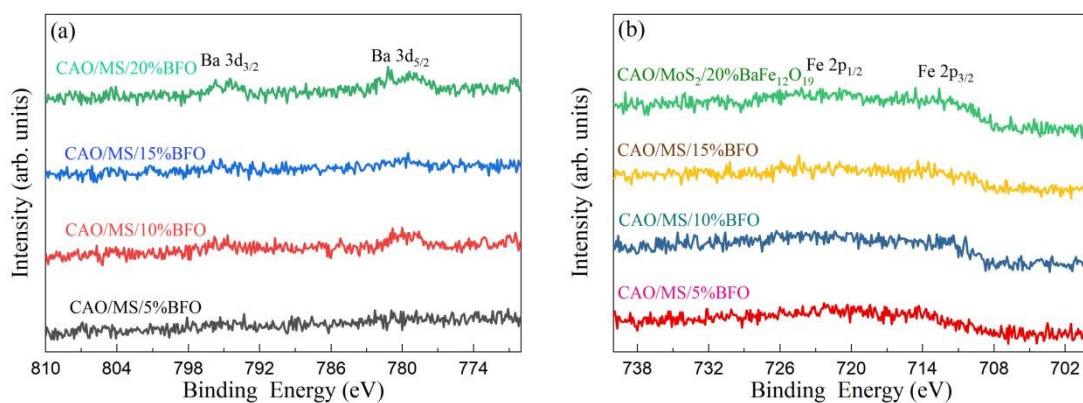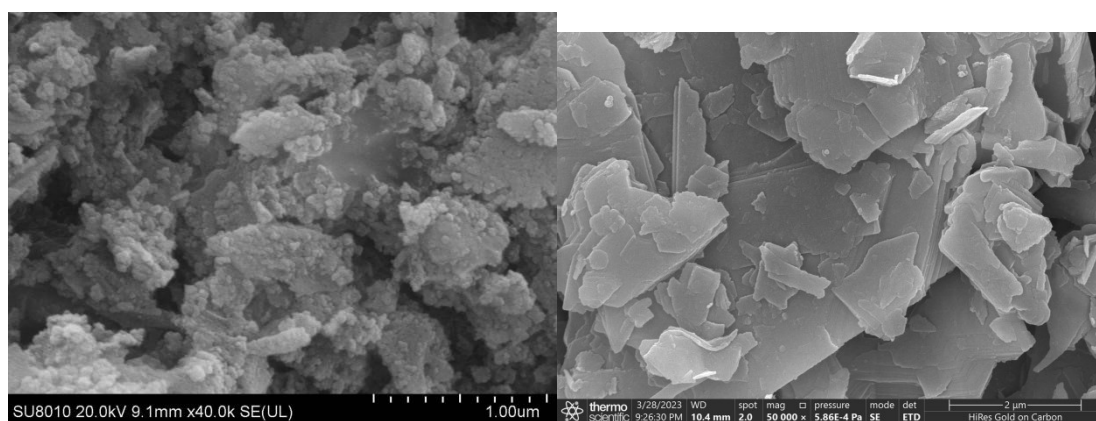CAO/MS/5%BFO, (b) CAO/MS/10%BFO, (c) CAO/MS/15%BFO and (d)

CAO/MS/20%BFO.

Figure S7 High-resolution (a) Ba 3d and (b) Fe 2p spectra of CAO/MS/BFO magnetic

photocatalysts.

Figure S7(a) shows the high-resolution Ba 3d spectra of CAO/MS/BFO magnetic

photocatalysts. For the Ba 3d spectra, the peaks of Ba 3d3/2 and Ba 3d5/2 locate at

794.78-795.17 and 779.81-780.11 eV, respectively, indicating that the Ba ion mainly
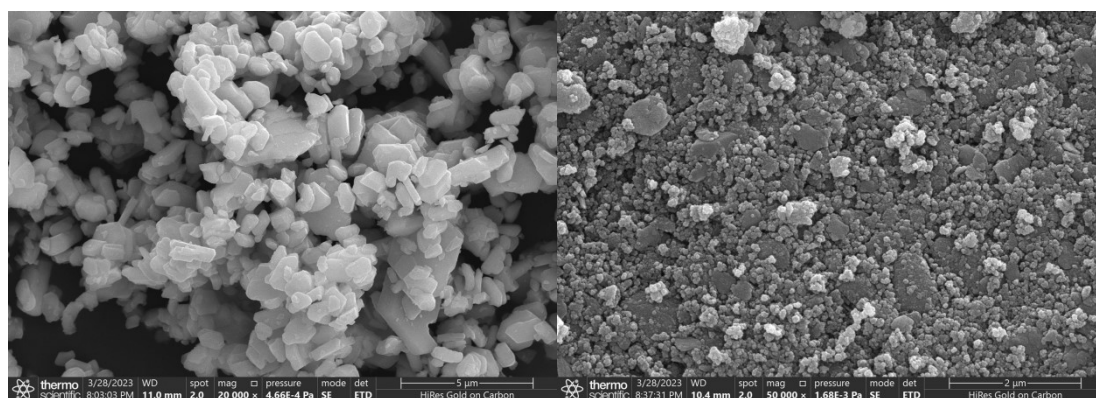
exists in the form of Ba^{2+} in BFO. [S5-S7] Figure S7(b) depicts the high-resolution Fe 2p XPS spectra of the CAO/MS/BFO magnetic photocatalysts, which can be deconvoluted into two peaks at 711.14-711.90 and 724.47-725.56 eV corresponding to Fe 2p2/3 and Fe 2p1/2 in BFO photocatalysts, respectively.

S4 Microstructural analysis

(a)　　　　　　　　　　　　　　　　　(b)

(c)　　　　　　　　　　　　　　　　　(d)

Figure S8 SEM images of (a) CAO, (b) MS, (c) BFO, and (d) CAO/10%MS.

S5 Optical properties

(a)   (b)   (c)   (d)

Figure S9 Real color photos of (a) CAO/MS/5%BFO, (b) CAO/MS/10%BFO, (c) CAO/MS/15%BFO and (d) CAO/MS/20%BFO photocatalysts.
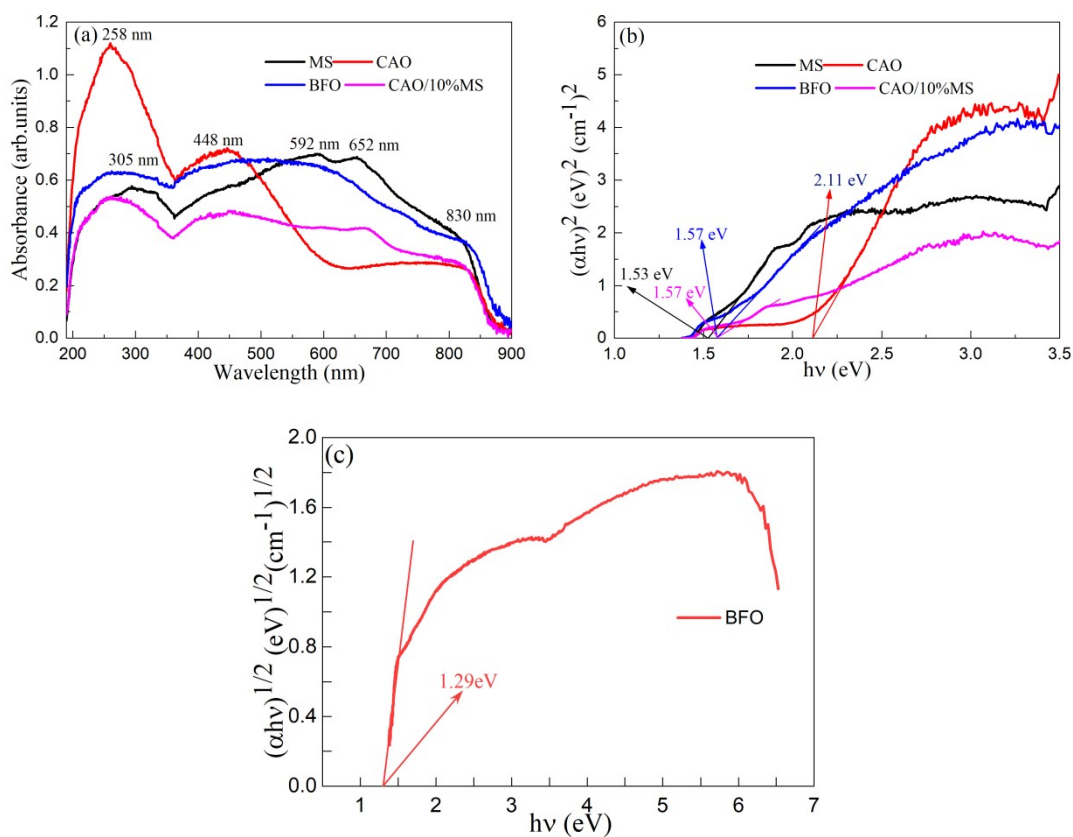

Figure S10 (a) UV - vis ABS spectra and (b) Tauc plots of CAO, MS, BFO, and CAO/10%MS photocatalysts for the direct band gap. (c) The $(\alpha h\nu)^{1/2}$ versus $h\nu$ curve of BFO photocatalyst for the indirect band gap.

For the MoS_2 photocatalysts, four obvious absorption peaks at 305, 442, 592 and 652 nm can be observed corresponding to the direct transition from the deep valence

band to the conduction band and rising from the K point of the Brillouin zone. As shown in Figure S10(a), there are three absorption peaks at 258, 448 and 700 nm in CuAl$_2$O$_4$, implying that the CuAl$_2$O$_4$ oxides has different optical transition with the different tops of valence band and bottoms of conduction band and the transition of Cu^{2+} in the distorted octahedron.

Based on the DRS annd the formula (S2), the color parameters (L*, a*, b*) of the CAO, MS, BFO, CAO/10%MS, CAO/MS/5%BFO, CAO/MS/10%BFO, CAO/MS/15%BFO and CAO/MS/20%BFO photocatalysts can be calculated and given in Table S3.

$$\begin{cases} L^* = 116 \times (\dfrac{Y_{10}}{Y_n})^{\frac{1}{3}} - 16, \dfrac{Y_{10}}{Y_n} > 0.008856 \\[2mm] a^* = 500 \times [(\dfrac{X_{10}}{X_n})^{\frac{1}{3}} - (\dfrac{Y_{10}}{Y_n})^{\frac{1}{3}}], \dfrac{X_{10}}{X_n} > 0.008856 \\[2mm] b^* = 200 \times [(\dfrac{Y_{10}}{Y_n})^{\frac{1}{3}} - (\dfrac{Z_{10}}{Z_n})^{\frac{1}{3}}], \dfrac{Z_{10}}{Z_n} > 0.008856 \end{cases} \qquad (S2)$$

Where, (X$_n$, Y$_n$, Z$_n$) = (94.81, 100, 107.32). Based on formula (7), (X$_{10}$, Y$_{10}$, Z$_{10}$) can be estimated.

$$\begin{cases} X_{10} = \dfrac{100 \times \sum R(\lambda) \times S(\lambda) \times x_{10}(\lambda) \times \Delta\lambda}{\sum S(\lambda) \times y_{10}(\lambda) \times \Delta\lambda} \\[3mm] Y_{10} = \dfrac{100 \times \sum R(\lambda) \times S(\lambda) \times y_{10}(\lambda) \times \Delta\lambda}{\sum S(\lambda) \times y_{10}(\lambda) \times \Delta\lambda} \\[3mm] Z_{10} = \dfrac{100 \times \sum R(\lambda) \times S(\lambda) \times z_{10}(\lambda) \times \Delta\lambda}{\sum S(\lambda) \times y_{10}(\lambda) \times \Delta\lambda} \end{cases} \qquad (S3)$$

Where, λ, (x$_{10}(\lambda)$, y$_{10}(\lambda)$, z$_{10}(\lambda)$), S(λ), R(λ) and $\Delta\lambda$ is the wavelength, the color matching function, the relative spectral power distribution, the reflectance, and 1 nm, respectively.

Table S3 Color related parameters and Eg values of CAO, MS, BFO, CAO/10%MS, CAO/MS/5%BFO, CAO/MS/10%BFO, CAO/MS/15%BFO and CAO/MS/20%BFO photocatalysts.

Sample	Color coordinates						Eg value (eV)
	L^*	a^*	b^*	c^*	H^o	ΔE_{CIE}^*	
CAO	67.877	12.102	26.837	29.439	65.727	73.986	2.11
MS	53.743	1.045	-8.202	8.268	-82.739	54.375	1.53
BFO	53.916	2.941	0.585	2.999	11.255	53.999	1.57/1.29
CAO/10% MS	67.214	0.925	4.096	4.199	77.274	67.345	1.57
CAO/MS/ 5%BFO	87.742	0.252	0.568	0.621	66.075	87.744	2.50
CAO/MS/ 10%BFO	72.776	0.410	1.446	1.503	74.171	72.792	2.87
CAO/MS/ 15%BFO	87.852	0.836	1.491	1.709	60.714	87.869	2.56
CAO/MS/ 20%BFO	79.041	0.900	1.133	1.447	51.541	79.054	2.67

L^*- black (0) / white (100), a^*-green (-) / red (+), b^*-blue (-) / yellow (+).
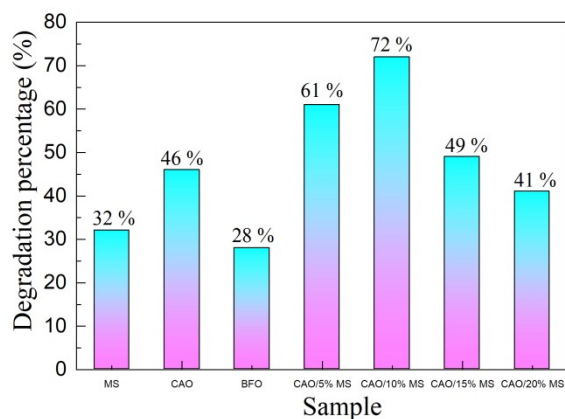
S6 Photocatalytic activity

Figure S11 Degradation percentage of MS, CAO, BFO, and CAO/MS photocatalysts

($C_{Catalyst}$=1 g/L, C_{TC}=100 mg/L and pH=11).

Figure S11 shows the degradation percentage of MS, CAO, BFO, and CAO/MS photocatalysts. The degradation percentage of MS, CAO, BFO, and CAO/5%MS, CAO/10%MS, CAO/15%MS and CAO/20%MS photocatalysts are 32%, 46%, 28%, 61%, 72%, 49% and 41%, respectively.
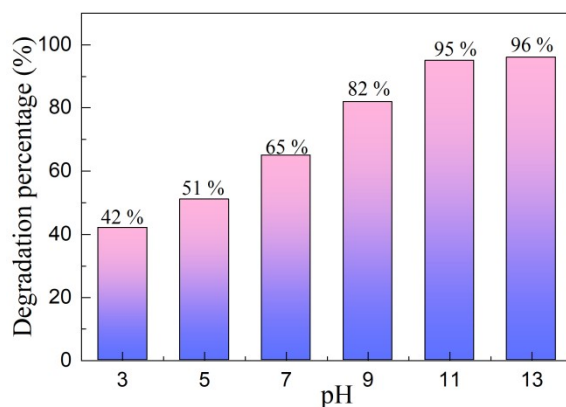

Figure S12 Effect of pHs. C_{TC}=100 mg/L, $C_{Photocatalyst}$=1 g/L.
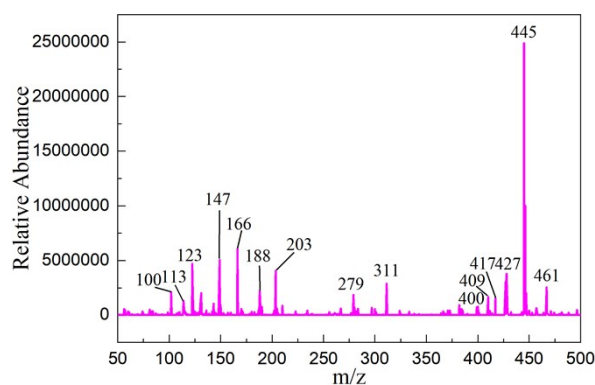
S7 LC-MS spectrum

Figure S13 The HPLC-MS spectra of TC degradation process.

S8 First principle calculations

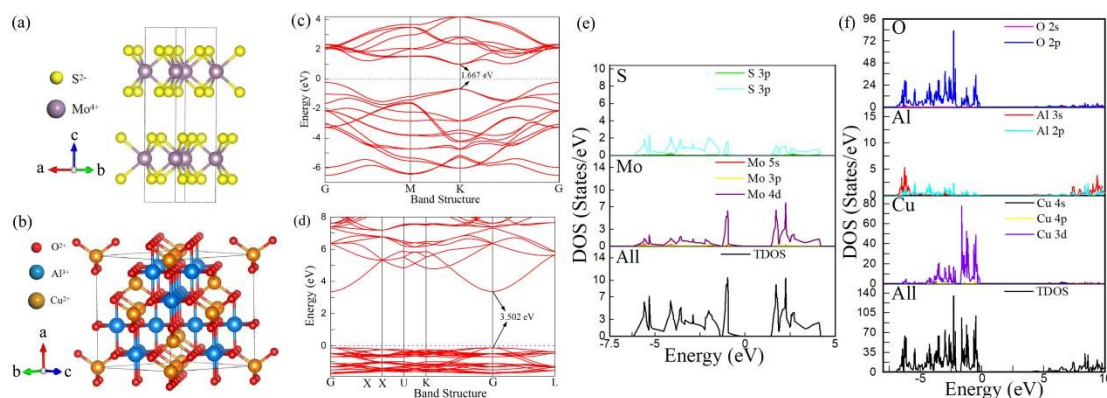Figure S14 (a, b) Crystal structures, (c, d) Electronic structures and (e, f) Density of states of $CuAl_2O_4$ and MoS_2.

The electron structure and electron state density of MoS_2 and $CuAl_2O_4$ are calculated theoretically by first principles. Using Vienna ab into simulation package (VASP) as a calculation tool, the Perdew-Burke-Ernzerth (PBE) exchange correlation functional of generalized gradient approximation (GGA) is used to study the electronic structure and electron state density of $CuAl_2O_4$ and MoS_2. Figure S14(a) shows the crystal structure of MoS_2. MoS_2 is a hexagonal structure with space group P63/mmc, and its lattice constants of a=b= 3.19 Å and c= 13.38 Å, and the crystal plane angle of α=β=90° and γ=120°. Figure S14(b) shows the crystal structure of $CuAl_2O_4$. The selected $CuAl_2O_4$ cell is a cubic structure with lattice constant of a=b=c= 8.06 Å and the crystal plane angle α=β=γ=90°. It contains 56 atoms and space

group is Fd3m. To achieve the purpose of structural optimization, the convergence standard of energy and force is set to 10 E^{-4} and -0.02 eV, respectively. The plane wave cutoff energy is set to 600 eV. The Monkhorst-Pack k-point meshes of MoS_2 and $CuAl_2O_4$ are set to $4\times4\times2$ and $3\times3\times3$, respectively. Then, the subsequent calculation is carried out on the basis of the convergence structure. Figure S14(c) and Figure S14(d) are the electronic structures of MoS_2 and $CuAl_2O_4$, respectively. The conduction band bottom and valence band top of MoS_2 and $CuAl_2O_4$ are located in the same wave vector space, indicating that both semiconductor materials are direct bandgap semiconductors. The optical band gap values of MoS_2 and $CuAl_2O_4$ are 1.667 and 3.502 eV, respectively. The optical band gap value of MoS_2 is basically consistent with the experimental value reported in the literature, but the optical band gap value of $CuAl_2O_4$ is very different from the experimental value, mainly for two reasons: First, there is a small amount of adsorbed oxygen on the surface of $CuAl_2O_4$ in this experiment, which will reduce the optical band gap value of $CuAl_2O_4$. Second, different preparation methods have great influence on the optical band gap value of $CuAl_2O_4$. Figure S14(e) and Figure S14(f) are electron state density of MoS_2 and $CuAl_2O_4$, respectively. The main electron orbitals in MoS_2 and $CuAl_2O_4$ are S 3p and Mo 4d orbitals and O 2p and Cu 3d orbitals, respectively.
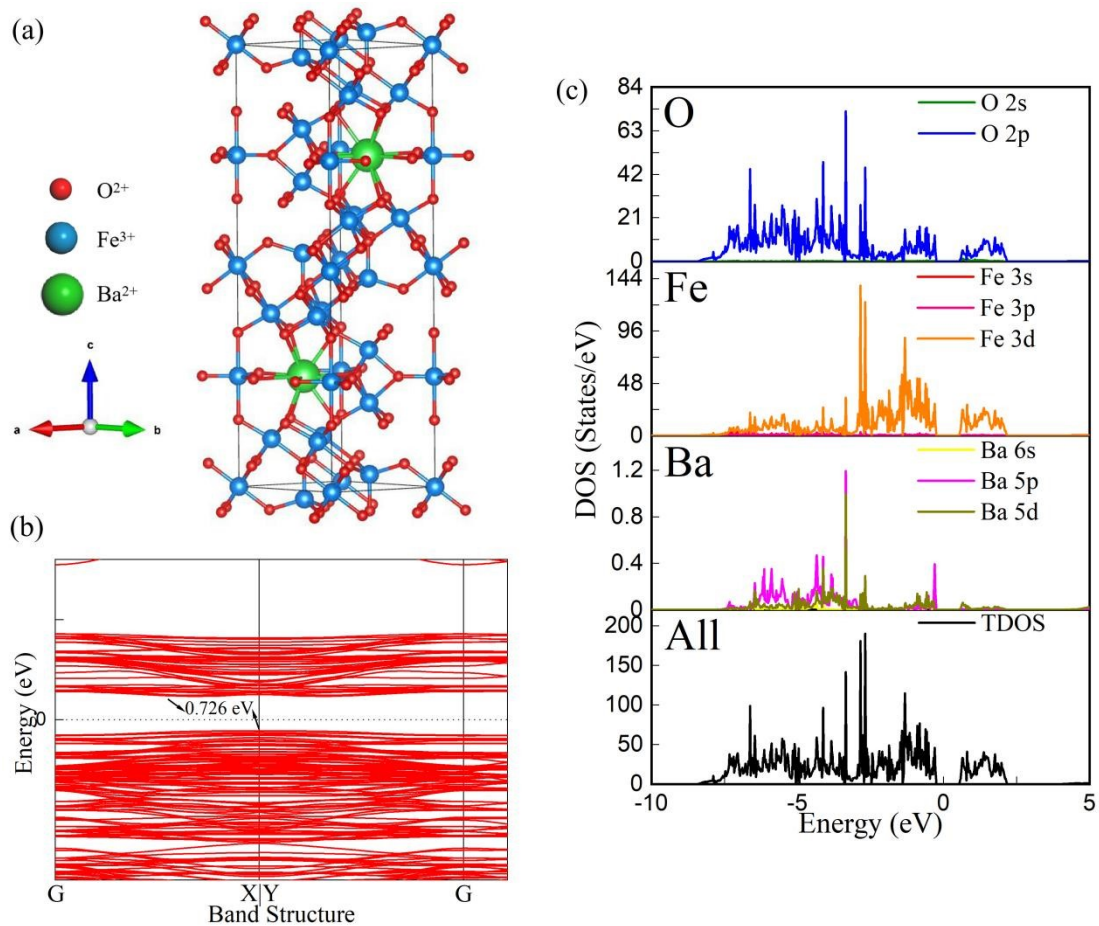
Figure S15 (a) Crystal structure, (b) electronic structure and (c) density of state of

BFO.

The unit cell of BFO used for calculation has a hexagonal structure, the space group is F63/mmc, the lattice parameters are a=b= 6.02 Å, c= 23.50 Å and the angle between crystal axes are α=β=90°, γ=120°, as shown in Figure S15(a). Figure S15(b) shows the electronic structure diagram of BFO hexagonal ferrite, which has a Eg value of 0.726 eV, which is smaller than the Eg value tested in the experiment, because the PBE functional will underestimate the calculated Eg value, so there is a certain deviation from the experimental value. Figure S15(c) displays the DOS diagram of hexaferrite BFO. As can be seen from Figure S15(c), both the conduction and valence bands of BFO are occupied by O 2p and Fe 3d orbitals.

References

[S1] J. Zhang, C. Shao, X. Li, J. Xin, S. Yang and Y. Liu, Electrospun $CuAl_2O_4$ hollow nanofibers as visible light photocatalyst with enhanced activity and excellent stability under acid and alkali conditions, *Crystengcomm*, 2018, **20**, 312-322.

[S2] A. Amri, X. Duan, C. Yin, Z. Jiang, M. M. Rahman and T. Pryor, Solar absorptance of copper–cobalt oxide thin film coatings with nano-size, grain-like morphology: optimization and synchrotron radiation XPS studies, *Appl. Surf. Sci.*, 2013, **275**, 127-135.

[S3] Y. Lu, L. Xu and C. Liu, Magnetically separable and recyclable photocatalyst MoS_2-$SrFe_{12}O_{19}$ with p-n heterojunction: Fabrication, characterization, and photocatalytic mechanism, *Appl. Organomet. Chem.*, 2020, **34**, e5288.

[S4] X. Q. Qiao, F. C. Hu, F. Y. Tian, D. F. Hou and D. S. Li, Equilibrium and kinetic studies on MB adsorption by ultrathin 2D MoS_2 nanosheets, *RSC Adv.*, 2016, **6**, 11631-11636.

[S5] S. F. Wang, X. Y. Chen, L. M. Fang, H. J. Gao, M. J. Han, X. P. Chen, Y. H. Xia, L. Xie and H. Yang, Double heterojunction $CQDs/CeO_2/BaFe_{12}O_{19}$ magnetic separation photocatalysts: Construction, structural characterization, dye and POPs removal, and the interrelationships between magnetism and photocatalysis, *Nuclear Analysis*, 2022, **1**, 100026.

[S6] F. F. Hu, H. Nan, M. Q. Wang, Y. Lin, H. B. Yang, Y. Qiu and B. Wen, Construction of core-shell $BaFe_{12}O_{19}$@ MnO_2 composite for effectively enhancing microwave absorption performance, *Ceram. Int.*, 2021, **47**, 16579-16587.

[S7] J. Y. Choi, J. M. Lee, Y. K. Baek, J. G. Lee and Y. K. Kim, The structural and magnetic properties of $BaFe_{12}O_{19}$ nanoparticles: effect of residual sodium ions, *Dalton T.*, 2021, **50**, 14560-14565.